AGU100 ADVANCING EARTH AND SPACE SCIENCE

Geophysical Research Letters

RESEARCH LETTER
10.1029/2018GL078602

Special Section:
Cassini's Final Year: Science Highlights and Discoveries

Key Points:
- Computation of Tethys albedo maps at VIS and IR wavelengths by means of photometric correction
- Retrieval of visible spectral slopes and water ice band depth maps
- Study of the correlations between spectral maps and geomorphological features

Correspondence to:
G. Filacchione,
gianrico.filacchione@iaps.inaf.it

Citation:
Filacchione, G., Ciarniello, M., D'Aversa, E., Capaccioni, F., Cerroni, P., Buratti, B., et al. (2018). Photometric modeling and VIS-IR albedo maps of Tethys from Cassini-VIMS. *Geophysical Research Letters*, *45*, 6400–6407. https://doi.org/10.1029/2018GL078602

Received 6 MAY 2018
Accepted 11 JUN 2018
Accepted article online 19 JUN 2018
Published online 7 JUL 2018

Photometric Modeling and VIS-IR Albedo Maps of Tethys From Cassini-VIMS

G. Filacchione[1], M. Ciarniello[1], E. D'Aversa[1], F. Capaccioni[1], P. Cerroni[1], B. Buratti[2], R. N. Clark[3], K. Stephan[4], and C. Plainaki[5]

[1]Istituto di Astrofisica e Planetologia Spaziali, INAF, Rome, Italy, [2]Jet Propulsion Laboratory, California Institute of Technology, Pasadena, CA, USA, [3]Planetary Science Institute, Tucson, AZ, USA, [4]German Aerospace Center (DLR), Berlin, Germany, [5]Italian Space Agency (ASI), Rome, Italy

Abstract We report about the derivation of visible (VIS) and infrared (IR) albedo maps and spectral indicators of Saturn's satellite Tethys from the complete Cassini-Visual and Infrared Mapping Spectrometer (VIMS) data set. The application of a photometric correction is necessary to remove illumination and viewing effects from the I/F spectra, to compute spectral albedo and to correctly associate spectral variations to changes in composition or physical properties of the surface. In this work we are adopting the photometric correction proposed by Shkuratov et al. (2011, https://doi.org/10.1016/j.pss.2011.06.011) to derive albedo maps of Tethys from disk-resolved Cassini-VIMS data. After having applied a similar methodology to Dione's data (Filacchione et al., 2018, https://doi.org/10.1002/2017GL076869), we present here the results achieved for Tethys: surface albedo maps and photometric parameters are computed at five visible (0.35, 0.44, 0.55, 0.70, and 0.95 μm) and five infrared (1.046, 1.540, 1.822, 2.050, and 2.200 μm) wavelengths and rendered in cylindrical projection with a 0.5° × 0.5° angular resolution in latitude and longitude, corresponding to a highest spatial resolution of 4.7 km/bin. The 0.35- to 0.55- and 0.55- to 0.95-μm spectral slopes and the water ice 2.050-μm band depth maps are computed after having applied the photometric correction, in order to trace the leading-trailing hemisphere dichotomy, to constrain the shape of the equatorial lens generated by the bombardment of high-energy magnetospheric electrons on the leading hemisphere, and to observe the stronger water ice band depth and reddening within the floors of Odysseus and Penelope impact craters.

Plain Language Summary Visible and infrared albedo maps of Tethys surface are derived from Cassini-Visual and Infrared Mapping Spectrometer data set by applying a photometric correction able to remove illumination and viewing effects from the data. This processing allows to build spectral indicator maps able to trace composition changes in terms of visible colors and water ice band depth across the surface. We focus our analysis on specific geologic features, including impact craters and low-albedo areas, where exogenic processes are occurring. We report how E-ring particles, magnetospheric and cold plasma particles bombardment, alter the surface of Tethys.

1. Introduction

This letter is the second of a series reporting photometric corrected maps of Saturn's icy satellite surfaces from Cassini/Visual and Infrared Mapping Spectrometer (VIMS) data (Brown et al., 2004). After having described the photometric correction method introduced by Shkuratov et al. (2011) applied to Dione's data set (Filacchione et al., 2018), we continue to use a similar methodology for Tethys' data set.

Tethys is characterized by a high geometric albedo of 1.23 at 0.55 μm (the brighter Enceladus is at 1.38; Verbiscer et al., 2007) and a bolometric bond albedo of 0.61 ± 0.09 (Pitman et al., 2010). Moreover, the satellite has a low density, 0.98 g/cm^3 (Thomas, 2010), indicative of a bulk composition mainly made of water ice and small amount of rocky material. The surface of the moon shows different geological units (Stephan et al., 2016), including large impact craters, such as Odysseus on the north hemisphere, high cratered terrains, and large areas affected by tectonism such as Ithaca Chasma, a trough feature which extends for about three fourths of the satellite's circumference with a maximum depth of about 3 km and a width from a few to about a hundred kilometers (Jaumann et al., 2009). A detailed description of Tethys properties derived

from Cassini in the context of the Saturnian moons system is given in Jaumann et al. (2009), while geologic maps of the moon's surface derived from Cassini Imaging Science Subsystem (ISS) and VIMS observations have been published by Roatsch et al. (2009, 2009). Global compositional maps of Tethys from VIMS data derived in the past by Stephan et al. (2016), without applying any specific photometric correction, have allowed for the characterization of the properties at hemispheric scale and the study of relationships between spectral classes and geological units at local scales. At global scale, VIMS data have been exploited to measure Tethys' disk-integrated colors and water ice band properties from observations taken from a wide range of illumination and viewing geometries (Filacchione et al., 2007, 2010, 2012) and to trace the spectral variability of chromophores and water ice in the context of Saturn's icy satellites and ring system (Filacchione et al., 2013). In a recent study (Hendrix et al., 2018), UV, visible, and IR data are synergistically used to derive geometric albedos of the icy satellites and to correlate surface color variations with the deposition of E-ring particle, which contain a weathered organic material fraction. The observed reddening radial trend, which increases from Enceladus to Rhea (Filacchione et al., 2013), could therefore be the consequence of the weathering by magnetospheric particles of the organic material embedded in the E-ring particles; the reddening increases with the age of the E-ring grains, and as a result, the grains impacting on Rhea's surface are much redder than those falling on inner moons. The reference albedo color map of Tethys has been derived from ISS camera color images by Schenk et al. (2011). The map is photometrically corrected at visible wavelengths reaching a spatial resolution of 1–1.5 km/pixel over the entire surface of the satellite. ISS map clearly shows the presence of prominent global asymmetries in both color and albedo with the darkest and reddest units observed on the middle of the trailing hemisphere (longitude = 270°) caused by interaction with magnetospheric cold plasma and/or deposition of small dark particles. The leading hemisphere is in general affected by the deposition of E-ring water ice particles. A dark and bluish lens caused by the bombardment of high-energy electrons embedded in Saturn's magnetosphere is observed on the equatorial region of the leading hemisphere.

In this work we aim to use the complete VIMS data set and to apply a photometric correction in order to build visible-near-infrared albedo and spectral indicators maps of Tethys and to give an interpretation of the results for resolved geologic features.

2. Observations and Data Selection

During the entire Cassini mission (2004–2017) VIMS has acquired Tethys surface observations on more than 280,000 pixels from a very wide range of distances, illumination, and observation conditions. Among those, in this work we have selected about 110,000 pixels that simultaneously fulfill the following conditions: (1) they have an unsaturated signal (≤4,000 DN); (2) they have an incidence angle i≤ 80°, an emission angle e ≤ 80°, and a phase angle 10° ≤ g ≤ 70°; (3) they are acquired from distances ≤100,000 km, corresponding to a spatial resolution better than 50 km/pixel in nominal resolution mode and 17 or 17 × 25 km/pixel in high-resolution mode respectively for the VIS and IR channels. This choice allows us to remove pixels acquired at very oblique views and in the opposition effect regime, which cannot be corrected by the photometric model we are adopting. VIMS-IR data are calibrated in I/F according to RC17 pipeline (Clark et al., 2012). VIMS-VIS data are calibrated following the methods described in (Filacchione, 2006; Filacchione et al., 2007). The geometry information associated to each VIMS pixel has been derived by a proprietary software based on the reconstructed SPICE kernels (Acton, 1996) of the Cassini mission.

3. Photometric Correction

The details of the method used to determine the photometric correction are fully described in Filacchione et al. (2018) and are not repeated here for the sake of brevity.

The photometric fit parameters a, b, c (see equation (5) in Filacchione et al., 2018) and statistical errors for each of them are listed in Table 1. Due to long computation times, the analysis has been performed only on five visible (0.35, 0.44, 0.55, 0.70, 0.95 μm) and five infrared (1.046, 1.540, 1.822, 2.050, 2.200 μm) wavelengths, which means 10 out of the 352 VIMS spectral bands. We remark that this approach does not accounts for the opposition surge effect: for this reason, the computed equigonal albedo turns out to be lower than the normal albedo $A(\lambda, g)$, which is defined at $g = 0°$ and $i = e$ (Hapke, 1993).

The photometric correction shows further limitations which need to be considered in analyzing the derived albedo maps: (1) the disk function $D(i, e, g)$ is computed by assuming a spherical shape since a detailed digital

Table 1
Photometric Fit Parameters for the Ten Visible and Infrared Channels Used to Render Albedo Maps Shown in Figures 1 and 2

Wavelength (μm)	*a*	*b*	*c*
0.35	0.75042 ± 0.00106	$-5.7173 \cdot 10^{-3} \pm 3.63 \cdot 10^{-5}$	$5.9202 \cdot 10^{-6} \pm 2.85 \cdot 10^{-7}$
0.44	0.77108 ± 0.00100	$-4.8690 \cdot 10^{-3} \pm 3.45 \cdot 10^{-5}$	$-1.5032 \cdot 10^{-6} \pm 2.71 \cdot 10^{-7}$
0.55	0.79707 ± 0.00111	$-4.7057 \cdot 10^{-3} \pm 3.83 \cdot 10^{-5}$	$-3.0856 \cdot 10^{-6} \pm 3.01 \cdot 10^{-7}$
0.70	0.76842 ± 0.00110	$-4.0931 \cdot 10^{-3} \pm 3.80 \cdot 10^{-5}$	$-6.4263 \cdot 10^{-6} \pm 2.97 \cdot 10^{-7}$
0.95	0.74823 ± 0.00102	$-3.1529 \cdot 10^{-3} \pm 3.53 \cdot 10^{-5}$	$-1.2415 \cdot 10^{-5} \pm 2.78 \cdot 10^{-7}$
1.046	0.74563 ± 0.00174	$-2.3805 \cdot 10^{-3} \pm 6.07 \cdot 10^{-5}$	$-2.0830 \cdot 10^{-5} \pm 4.96 \cdot 10^{-7}$
1.540	0.45171 ± 0.00090	$-3.9953 \cdot 10^{-3} \pm 3.10 \cdot 10^{-5}$	$8.0352 \cdot 10^{-6} \pm 2.43 \cdot 10^{-7}$
1.822	0.70383 ± 0.00160	$-3.9038 \cdot 10^{-3} \pm 5.50 \cdot 10^{-5}$	$-5.0489 \cdot 10^{-6} \pm 4.30 \cdot 10^{-7}$
2.050	0.35282 ± 0.00059	$-4.9093 \cdot 10^{-3} \pm 2.07 \cdot 10^{-5}$	$2.2163 \cdot 10^{-5} \pm 1.64 \cdot 10^{-7}$
2.200	0.68231 ± 0.00127	$-5.0104 \cdot 10^{-3} \pm 4.37 \cdot 10^{-5}$	$5.4471 \cdot 10^{-6} \pm 3.42 \cdot 10^{-7}$

Note. The parameter *a* is the equigonal albedo value as defined in Filacchione et al. (2018).

shape model of the entire surface is not available. As a consequence of this, for rough morphologies, like on Ithaca Chasma or on Odysseus crater rim, the computation of the incidence and emission angles is not reliable and photometric residuals appear on the maps. In particular, the poor characterization of the incidence angles also does not permit to completely filter out unilluminated pixels; (2) the choice to selecting wide-angle (i, e, g) intervals allows to maximize the spatial coverage, but it implies a not uniform correction toward extreme illumination/viewing geometries (discussed in section 4).

4. Albedo Maps

The method used to render albedo maps from single observations is described in Filacchione, Capaccioni, et al. (2016), Filacchione, D'Aversa, et al. (2016): each individual VIMS pixel, fulfilling the filtering conditions discussed in section 2, is calibrated in I/F and then photometrically corrected by means of the phase function $F(\lambda, g)$ value computed with the coefficients reported in Table 1 and by the disk function $D(i, e, g)$ value. The resulting albedo is projected on the area defined by the four corners of the individual pixel on a cylindrical grid rendered with a spatial sampling of 0.5° × 0.5° per bin along west longitude and latitude axes. This sampling corresponds to a spatial resolution of 4.7 km/bin at the equator. A similar procedure is followed independently for each wavelength. Since VIMS VIS and IR channels have different radiometric response and instantaneous field of view, the resulting coverage can be slightly different from wavelength to wavelength. In case of redundancy above a given 0.5° × 0.5° per bin, the average value is shown on the albedo map in Figure 1a.

Tethys visible albedo color map covers all longitudes, with the exception of a gap in the middle of the trailing hemisphere, and almost all latitudes between ±80°. The albedo varies between 0.62 and 0.83 at 0.44 μm (band *B*), 0.68–0.87 at 0.55 μm (*G*), and 0.65–0.82 at 0.7 μm (*R*). The largest impact craters (Telemachus, Icarius, Ajax, Antinous, Penelope, Dolinus, Odysseus, and Anticleia), and Ithaca Chasma (see numerals on the map for their identification), and the low-albedo equatorial lens (Paranicas et al., 2014; Schenk et al., 2011) centered on the middle of the leading hemisphere (longitude = 90°) and caused by the bombardment of high-energy (>10 keV) electrons trapped in the Saturnian magnetosphere, are clearly visible. The lens encompasses the meridional rim of the large Odysseus crater and appears to be not completely symmetric with respect to the equator, but it is more extended toward northern latitudes (22°) than on southern (−15°) at longitude = 90° meridian. Despite the gap in the data coverage, the dark terrain area located on the middle of the trailing hemisphere (longitude = 270°) and encompassing Penelope, Ajax, Icarius, and Antinous craters appears visible on VIMS albedo map.

In general, ISS albedo map by Schenk et al. (2011) shown in Figure 1b appears more uniform than the VIMS one in both spatial resolution and photometric rendering. Along with the higher spatial resolution of ISS with respect VIMS, this is consequence of the broad filtering of the (i, e, g) angles ranges selected on VIMS data: for comparison, ISS albedo map was built with data taken on a very limited phase range (from 10° to 30°) applying empirical photometric correction. For the VIMS data set we have relaxed the filtering in the 10°–90° range to achieve a more extended spatial coverage. As a consequence of this choice, despite adopting a mathematical photometric correction, the rendering is progressively less accurate for high illumination and viewing angles

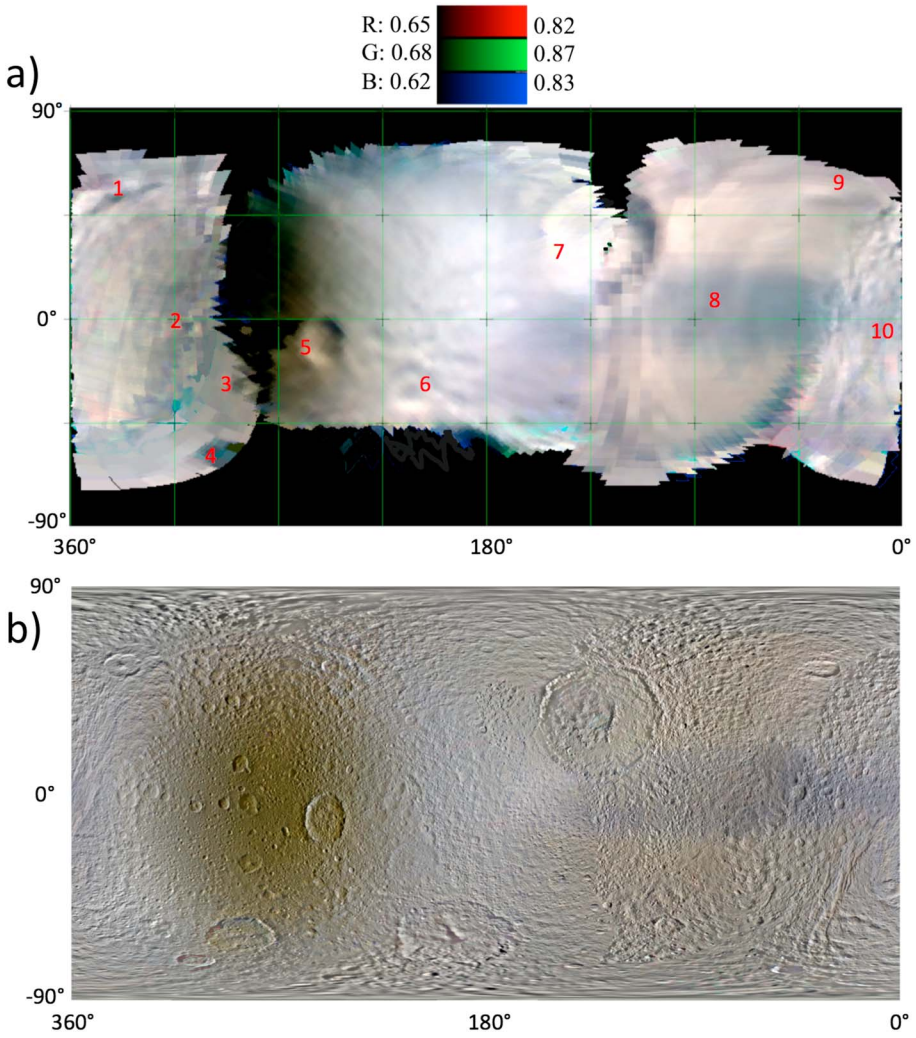

Figure 1. (a) Tethys visible color albedo map at $B = 0.44$ μm, $G = 0.55$ μm, and $R = 0.7$ μm. Numerals indicate the position of the principal geological features resolved on the map: (1) Telemachus crater, (2) Icarius, (3) Ajax, (4) Antinous, (5) Penelope, (6) Dolius, (7) Odysseus, (8) Dark Equatorial Lens, (9) Anticleia, and (10) Ithaca Chasma. (b) Cassini-ISS color map from Schenk et al. (2011).

resulting in some photometric residuals. The most evident of those residuals is the arc-shaped dark feature starting from the edge of the dark equatorial lens (at approximately longitude = 45° at the equator), running parallel to the south part of Ithaca Chasma and finishing at longitude = 90°, latitude = −55°.

The infrared albedo maps computed on a set of five wavelengths encompassing the center of the strongest water ice bands at 1.54 and 2.05 μm and local continuum at 1.82 and 2.20 μm are shown as separate panels in Figure 2. On the absorption bands the minimum albedo of 0.43 and 0.3 for the 1.54- and 2.05-μm wavelengths, respectively, is reached on the equatorial dark lens and toward the center of the trailing hemisphere (longitude = 270°). At the same wavelengths the maximum albedo is 0.61 and 0.38, respectively, measured on the north hemisphere, in particular at longitude = 45° for latitude ≥ 45° on the north of the Anticleia crater (label 9 in Figure 1). On the continuum wavelengths we observe a similar distribution but shifted toward higher albedo values, up to 0.95 and 0.88 at 1.82 and 2.2 μm, respectively. Moreover, the dark equatorial lens appears much more contrasted on the continuum rather than on the water ice absorption wavelengths: on the 1.82-μm continuum the lens minimum albedo is about 0.79, while the terrains immediately outside it are at 0.83; on the 2.05-μm water ice absorption the albedo is 0.32 within the lens and 0.33 outside it. If we assume that the observed water ice band depth distribution is only driven by grain size effects and not by a different abundance of contaminants within the lens, then a similar photometric behavior is compatible with a distribution of larger water ice grains in the lens area with respect to the north hemisphere region where

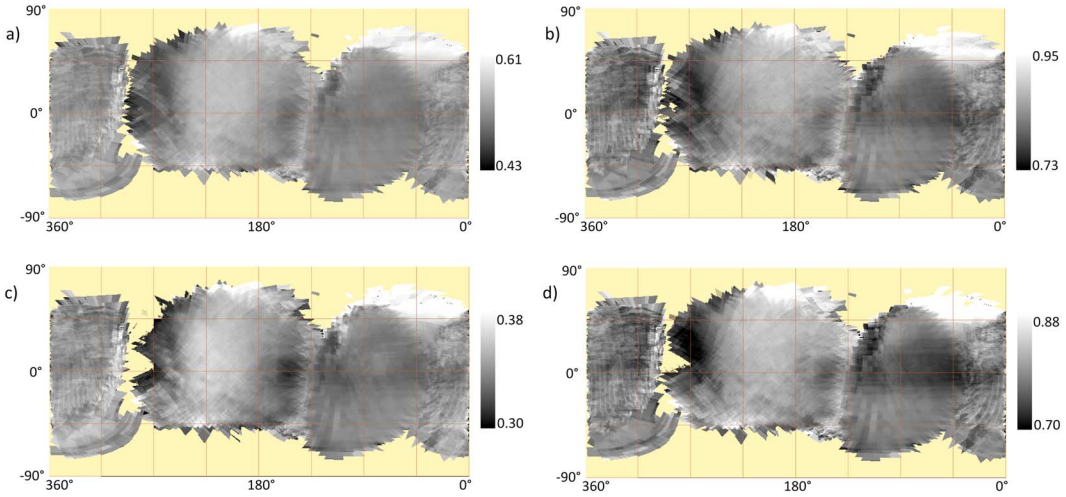

Figure 2. Tethys infrared albedo maps at 1.54 (a), 1.82 (b), 2.05 (c), and 2.20 μm (d).

the albedo is higher. As discussed in Filacchione et al. (2012), water ice particles with diameters of micron to tens of microns are characterized by higher albedo on the infrared continuum compared to larger grains (diameter of the order of hundred of microns to centimeters). The part of the Odysseus crater toward the leading hemisphere (longitude = 110°) appears darker at all four wavelengths: since a similar effect is seen also on the visible albedo map in Figure 1, this is probably a photometric residual due to the rough rim morphology and not a real feature. Conversely, the southernmost part of Ithaca Chasma (20° ≤ longitude ≤ 40°, −60° ≤ latitude ≤ −45°) appearing consistently darker on all four infrared maps but not in the visible seems to be a real albedo feature.

5. Spectral Indicator Maps

The 0.35- to 0.55- and 0.55- to 0.95-μm spectral slopes and 2-μm band depth (Filacchione et al., 2012) are spectral indicators suitable to study the relative amounts of compositional end-members (water ice and chromophores) and regolith grain size. These quantities are computed from the albedo, and the resulting maps are shown in Figure 3. The 0.35- to 0.55-μm slope map highlights the presence of the equatorial lens in great detail, visible as a blue shaded ellipse centered on the equator of the leading hemisphere (map in panel a): the slope is close to null on the center of the lens and increases up to ≈0.35 μm^{-1} on the edge of the lens. Similar to the visible albedo map, the slope shows an asymmetry in the latitudinal direction, with a prevalence toward the north hemisphere. On the lens region the focusing of magnetospheric particles flux has caused the sintering of the water ice grains resulting in the formation of a regolith layer made by larger grains. As a consequence of this alteration, changes in color (Schenk et al., 2011), thermal inertia (Howett et al., 2012), and diurnal temperature (Filacchione, D'Aversa, et al., 2016) are observed on this area. Moving toward the anti-Saturnian hemisphere the *pacman* feature, originally discovered on Composite Infrared Spectrometer (CIRS) temperature maps (Howett et al., 2012), is visible on the spectral slope map as a local maximum (rendered in red color). It encompasses the extension of the entire Odyseeus crater, which shows remarkably uniform red color (slope ≥0.35 μm^{-1}) on the floor and walls of the rim. The anti-Saturnian quadrant, between 135° ≤ longitude ≤ 215° is characterized by a low spectral slope, similar to the values measured within the lens (≤0.35 μm^{-1}). The circular low-albedo area centered on the middle of the trailing hemisphere visible in Figure 1 is characterized by a high spectral slope, which reaches the maximum reddening on the floor of the Penelope crater (0.7 μm^{-1}, label 5 in Figure 1). Within the limits of the map coverage, the reddening extends at least within −45° ≤latitude ≤ 55°. A low reddening (≤0.35 μm^{-1}) is measured above Ithaca Chasma.

The absolute variability of the 0.55- to 0.95-μm slope (Figure 3, map in panel b) is less than one half of the 0.35- to 0.55-μm slope resulting in a more noisy map. Nevertheless, spatial trends similar to the ones previously discussed continue to be visible: the equatorial lens shows a negative slope, between −0.15 and −0.1 μm^{-1} resulting in bluer slopes than the rest of the leading hemisphere, which is between −0.1 and −0.05 μm^{-1}. The anti-Saturnian hemisphere is the region where the minimum slope (−0.25 μm^{-1}) is measured. The 0.55- to 0.95- μm slope on the center of the trailing hemisphere is moderately negative (−0.15 and −0.1 μm^{-1})

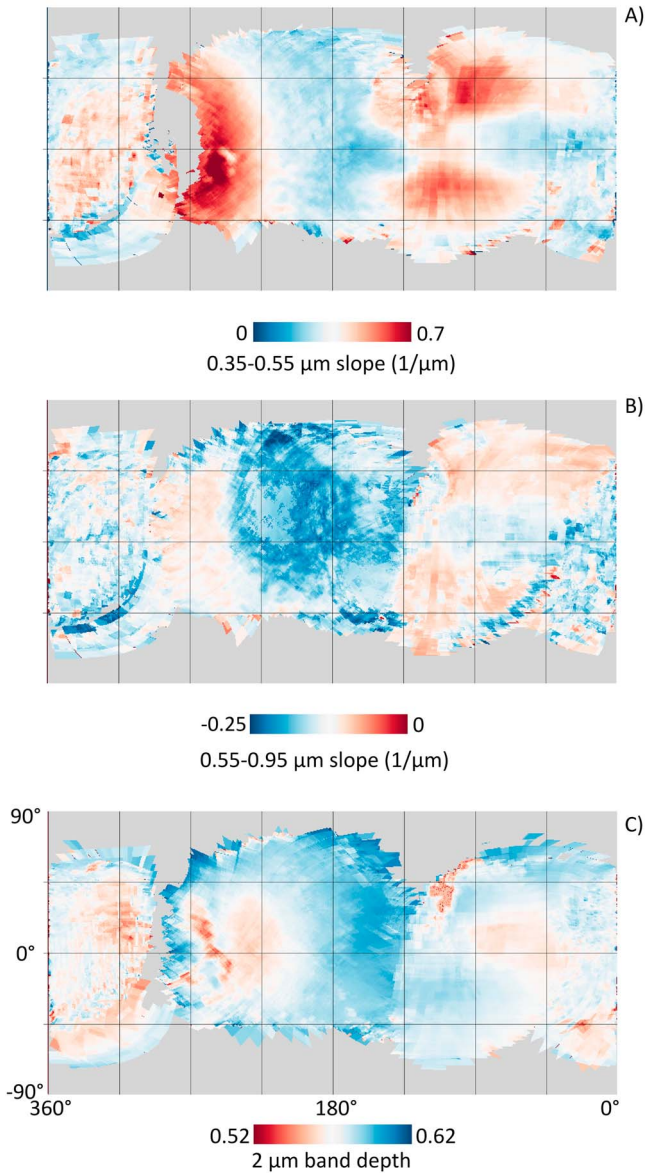

Figure 3. Tethys cylindrical maps for 0.35- to 0.55-μm slope (a), 0.55- to 0.95-μm slope (b), and 2-μm water ice band depth (c). The equatorial lens appears bluer than the rest of the leading hemisphere on the slopes maps. The band depth is minimum on the equatorial lens and across the trailing hemisphere.

and different from what seen on the 0.35- to 0.55-μm slope; the Penelope crater floor has a color similar to the surrounding terrains.

The 2-μm water ice band depth (Figure 3, map in panel c) shows a variability between 0.52 and 0.62: local band depth minima, rendered in red color, are measured within the equatorial lens on the leading hemisphere and on the majority of low-albedo units in the trailing (photometric residuals could affect some areas around longitude = 270° resulting in high band depth values). The maximum band depth, rendered in blue color, is seen on the anti-Saturnian quadrant and on the pacman feature and in general on the north hemisphere where the infrared albedo is maximum (as shown in white color on maps in Figure 2). Apart the variability observed at global scale, the map allows to appreciate the changes occurring on individual morphological features: (1) on the meridional part of Ithaca Chasma ($20° \leq$ longitude $\leq 40°$, $-60° \leq$latitude $\leq -45°$) a local minimum is observed, which seems to be correlated with the rough topography and low albedo at infrared wavelengths (Figure 2); (2) the floor of Odysseus crater has an high band depth; the lower values seen on the east rim could a photometric residual; (3) the floor of Penelope crater shows a remarkable increase of the band depth with respect to the nearby terrains; (4) high band depth is similarly seen on other impact craters like Telemachus and Anticleia (labels 1 and 9, respectively, in Figure 1a).

6. Discussion and Conclusions

By deriving photometric corrected albedo and spectral indicators maps of Tethys, we are able to trace the compositional changes occurring on the surface of the moon and to study the relationship between spectral indicators, exogenic processes, and morphological units. At visible colors VIMS data are in good agreement with high-resolution map by ISS (Schenk et al., 2011), allowing us to recognize the equatorial dark albedo lens on the leading hemisphere caused by the interaction with high-energy electrons trapped in Saturn's magnetosphere and the wide dark feature in the middle of the trailing hemisphere generated by the deposition of exogenic dark particles and cold plasma. The equatorial lens is likely related to the deposition of energy guided by asymmetric electron bombardment (Howett et al., 2011; Paranicas et al., 2012; Schenk et al., 2011). These high-energy electrons drift in a retrograde direction relative to corotation (Howett et al., 2012), and they preferentially impact low latitudes of Tethys' leading hemisphere (Paranicas et al., 2012). The dark feature of the trailing hemisphere may be generated by the deposition of nanophase grains or charged magnetospheric particles or both. We note, however, that the energetic protons of Saturn's magnetosphere have very low fluxes along the moon orbits (Kollmann et al., 2013). For example, the intensity of 1 MeV protons near the inner Saturnian satellites (Paranicas et al., 2012) is several orders of magnitude below the one at Ganymede (Paranicas et al., 2018). Moreover, whereas along the orbits of Janus, Mimas, and Enceladus, the proton fluxes were measured at low levels (macrosignatures), at Tethys (like Dione) no flux decrease effect has been observed, likely because of the faster radial transport there and the rate at which protons re-encounter that moon (see Figure 4 in Paranicas et al., 2018). As discussed in Hendrix et al. (2018), while the effect of surface's alteration caused by protons is negligible, the cold plasma embedded in Saturn's magnetosphere is the principal mechanism causing the darkening occurring on Tethys' trailing hemisphere.

While these two equatorial areas share common low visible and infrared albedos and low water ice band depth, they differ in visible colors, being the leading hemisphere equatorial lens remarkably blue while the trailing hemisphere appears very red. Such spectral differences are the consequence of the two very different alterations occurring on these areas. In particular, the bombardment of high-energy electrons is responsible of the alteration of the surface regolith grain size because the energy released by electrons is sintering

together ice grains resulting in the formation of larger grains. The low 2-μm band depth values observed within the leading hemisphere equatorial lens (Figure 3c) could be the consequence of this process rather than by a depletion of water ice content. A 2-μm band depth of 0.56 (supported by the 1.5-μm band of 0.34 derived from albedo maps in Figure 2) is compatible with the presence large water ice grains of the order of 1 cm (Filacchione et al., 2012). The presence of these large water ice particles is reinforced by the blue color of the lens in the visible range (panels a and b) and by the anomalous thermal behavior of the terrain within the lens (Filacchione, D'Aversa, et al., 2016; Howett et al., 2012). Moreover, we report about the asymmetric shape of the lens, which extends more on the north (22°) than on south (−15°) latitudes. Such a morphology could be the consequence of the disturbances occurring in the planetary magnetic field which is not well aligned starting from the orbit of Tethys. This misalignment affects how the electrons travel past the moon and where they preferentially impact the surface. It is therefore probable that local electromagnetics active in the vicinity of Tethys are the cause of the asymmetric shape of the lens (Paranicas et al., 2018). We note that the floors of several impact craters, mainly Penelope but also Odysseus, are remarkably red in the visible but have very high water ice band depth in the infrared. A similar behavior indicated the presence of exogenous chromophores especially on the trailing hemisphere low-albedo units. Finally, the north anti-Saturnian and leading hemisphere region are characterized by high infrared albedo (0.95 at 1.82 μm), intermediate visible color ($\leq$0.35 at 1 μm), and high water ice band depth (>0.59): these properties are indicative of the deposition of fine and bright water ice particles from the E-ring. After Dione and Tethys, we plan to use a similar methodology in the next future to the remaining Saturn's satellites.

Acknowledgments
The authors thank Amanda Hendrix and Chris Paranicas for the useful comments received during the review. The authors acknowledge the financial support from Italian Space Agency (ASI) for the Cassini-VIMS data analysis program. This research has made use of NASA's Astrophysics Data System. All data used in this work are publicly available through NASA-PDS.

References

Acton, C. (1996). Ancillary data services of NASA's navigation and ancillary information facility. *Planetary and Space Science*, *44*, 65–70.
Brown, R. H., Baines, K. H., Bellucci, G., Bibring, J.-P., Buratti, B. J., Capaccioni, F., et al. (2004). The Cassini visual and infrared mapping spectrometer (VIMS) investigation. *Space Science Reviews*, *115*, 111–168.
Clark, R. N., Cruikshank, D. P., Jaumann, R., Brown, R. H., Stephan, K., Dalle Ore, C. M. K., et al. (2012). The composition of Iapetus: Mapping results from Cassini VIMS. *Icarus*, *218*, 831–860.
Filacchione, G. (2006). Calibrazioni a terra e prestazioni in volo di spettrometri ad immagine nel visibile e nel vicino infrarosso per l'esplorazione planetaria (PhD thesis), Università di Napoli Federico II. Available from NASA-ADS.
Filacchione, G., Capaccioni, F., Ciarniello, M., Clark, R. N., Cuzzi, J. N., Nicholson, P. D., et al. (2012). Saturn's icy satellites and rings investigated by Cassini-VIMS: III—Radial compositional variability. *Icarus*, *220*, 1064–1096.
Filacchione, G., Capaccioni, F., Ciarniello, M., Raponi, A., Tosi, F., De Sanctis, M. C., et al. (2016). The global surface composition of 67P/CG nucleus by Rosetta/VIRTIS. (I) Prelanding mission phase. *Icarus*, *274*, 334–349.
Filacchione, G., Capaccioni, F., Clark, R. N., Cuzzi, J. N., Cruikshank, D. P., Coradini, A., et al. (2010). Saturn's icy satellites investigated by Cassini-VIMS. II. Results at the end of nominal mission. *Icarus*, *206*, 507–523.
Filacchione, G., Capaccioni, F., Clark, R. N., Nicholson, P. D., Cruikshank, D. P., Cuzzi, J. N., et al. (2013). The radial distribution of water ice and chromophores across Saturn's system. *The Astrophysical Journal*, *766*(2), 5.
Filacchione, G., Capaccioni, F., McCord, T. B., Coradini, A., Cerroni, P., Bellucci, G., et al. (2007). Saturn's icy satellites investigated by Cassini-VIMS. I. Full-disk properties: 350-5100 nm reflectance spectra and phase curves. *Icarus*, *186*, 259–290.
Filacchione, G., Ciarniello, M., D'Aversa, E., Capaccioni, F., Cerroni, P., Buratti, B. J., et al. (2018). Photometric modeling and VIS-IR Albedo maps of Dione from Cassini-VIMS. *Geophysical Research Letters*, *45*, 2184–2192. https://doi.org/10.1002/2017GL076869
Filacchione, G., D'Aversa, E., Capaccioni, F., Clark, R. N., Cruikshank, D. P., Ciarniello, M., et al. (2016). Saturn's icy satellites investigated by Cassini-VIMS. IV. Daytime temperature maps. *Icarus*, *271*, 292–313.
Hapke, B. (1993). *Theory of reflectance and emittance spectroscopy. Topics in remote sensing* (pp. c1993). Cambridge, UK: Cambridge University Press.
Hendrix, A. R., Filacchione, G., Paranicas, C., Schenk, P., & Scipioni, F. (2018). Icy Saturnian satellites: Disk-integrated UV-IR characteristics and links to exogenic processes. *Icarus*, *300*, 103–114.
Howett, C. J. A., Spencer, J. R., Hurford, T., Verbiscer, A., & Segura, M. (2012). PacMan returns: An electron-generated thermal anomaly on Tethys. *Icarus*, *221*, 1084–1088.
Howett, C. J. A., Spencer, J. R., Schenk, P., Johnson, R. E., Paranicas, C., Hurford, T. A., et al. (2011). A high-amplitude thermal inertia anomaly of probable magnetospheric origin on Saturn's moon Mimas. *Icarus*, *216*, 221–226.
Jaumann, R., Clark, R. N., Nimmo, F., Hendrix, A. R., Buratti, B. J., Denk, T., et al. (2009). Icy Satellites: Geological Evolution and Surface Processes. In M. K. Dougherty, L. W. Esposito, & S. M. Krimigis (Eds.), *Saturn from Cassini-Huygens* (pp. 637–681). Dordrecht, Heidelberg, London and New York: Springer.
Kollmann, P., Roussos, E., Paranicas, C., Krupp, N., & Haggerty, D. K. (2013). Processes forming and sustaining Saturn's proton radiation belts. *Icarus*, *222*, 323–341.
Paranicas, C., Hibbitts, C. A., Kollmann, P., Ligier, N., Hendrix, A. R., Nordheim, T. A., et al. (2018). Magnetospheric considerations for solar system ice state. *Icarus*, *302*, 560–564.
Paranicas, C., Roussos, E., Decker, R. B., Johnson, R. E., Hendrix, A. R., Schenk, P., et al. (2014). The lens feature on the inner Saturnian satellites. *Icarus*, *234*, 155–161.
Paranicas, C., Roussos, E., Krupp, N., Kollmann, P., Hendrix, A. R., Cassidy, T., et al. (2012). Energetic charged particle weathering of Saturn's inner satellites. *Planetary Space Sciences*, *61*, 60–65.
Pitman, K. M., Buratti, B. J., & Mosher, J. A. (2010). Disk-integrated bolometric Bond albedos and rotational light curves of Saturnian satellites from Cassini visual and infrared mapping spectrometer. *Icarus*, *206*, 537–560.
Roatsch, T., Jaumann, R., Stephan, K., & Thomas, P. C. (2009). Cartographic mapping of the Icy satellites using ISS and VIMS Data. In M. K. Dougherty, L. W. Esposito, & S. M. Krimigis (Eds.), *Saturn from Cassini-Huygens* (pp. 763–781). Dordrecht, Heidelberg, London and New York: Springer.

Roatsch, T., Wählisch, M., Hoffmeister, A., Kersten, E., Matz, K.-D., Scholten, F., et al. (2009). High-resolution Atlases of Mimas, Tethys, and Iapetus derived from Cassini-ISS images. *Planetary Space Science*, *57*, 83–92.

Schenk, P., Hamilton, D. P., Johnson, R. E., McKinnon, W. B., Paranicas, C., Schmidt, J., et al. (2011). Plasma, plumes and rings: Saturn system dynamics as recorded in global color patterns on its midsize icy satellites. *Icarus*, *211*, 740–757.

Shkuratov, Y., Kaydash, V., Korokhin, V., Velikodsky, Y., Opanasenko, N., & Videen, G. (2011). Optical measurements of the Moon as a tool to study its surface. *Planetary Space Sciences*, *59*, 1326–1371. https://doi.org/10.1016/j.pss.2011.06.011

Stephan, K., Wagner, R., Jaumann, R., Clark, R. N., Cruikshank, D. P., Brown, R. H., et al. (2016). Cassini's geological and compositional view of Tethys. *Icarus*, *274*, 1–22.

Thomas, P. C. (2010). Sizes, shapes, and derived properties of the Saturnian satellites after the Cassini nominal mission. *Icarus*, *208*, 395–401.

Verbiscer, A., French, R., Showalter, M., & Helfenstein, P. (2007). Enceladus: Cosmic graffiti artist caught in the act. *Science*, *315*, 815.